POTENTIAL UTILISATION FOR NANOTESTERS

PETR BOHAC*[a], RADIM CTVRTLIK[b], and MARTIN STRANYANEK[a]

[a] *Institute of Physics, AS CR, v.v.i, Na Slovance 2, Prague 8, Czech Republic,* [b] *Joint Laboratory of Optics, Palacky University and Institute of Physics AS CR, 17. listopadu 50, Olomouc, Czech Republic*
bohac@fzu.cz

Keywords: local mechanical properties, utilization of nanotester, DSI, XRD, nanocompression

1. Introduction

Hardness is defined as resistance of material to plastic deformation, usually by indentation. Two approaches to phenomenon named hardness have been developed for its application and explanation during last about one hundred years. Since beginning of the 20th century Brinell approached the problem as an engineer interested in comparing the properties of various materials, especially different batches of steel. The main role was adjudged to plastic deformation of materials caused by a hard asperity indented into a softer metal. The Brinell hardness test uses a desk top machine to press a 10 mm diameter, hardened steel ball into the surface of the test specimen. The machine applies a load of 5 kN for soft metals such as copper, brass and thin stock. A 15 kN load is used for aluminum castings, and a 30 kN load is used for materials such as iron and steel. The load is usually applied for 10 to 15 seconds. After the impression is made, a measurement of the diameter of the resulting round impression is taken. It is measured to plus or minus 0.05 mm using a low-magnification portable microscope. The hardness is calculated by dividing the load by the area of the curved surface of the indention.

The Rockwell hardness tester measures resistance to penetration like the Brinell test, but in the Rockwell case, the depth of the impression is measured rather than the diametric area. With the Rockwell tester, the hardness is indicated directly on the scale attached to the machine. This dial like scale is really a depth gauge, graduated in special units. The Rockwell hardness test is the most used and versatile of the hardness tests.

The Vickers testing method is similar to the Brinell test, but the Vickers machine uses a penetrator that is square in shape, but tipped on one corner so it has the appearance of a playing card "diamond". The Vickers indenter is a 136 degrees square-based diamond cone (or pyramid), the diamond material of the indenter has an advantage over other indenters because it does not deform over time and use. The impression left by the Vickers indenter is a dark square on a light background. The Vickers impression is more easily "read" for area size than the circular impression of the Brinell method. Like the Brinell test, the Vickers number is determined by dividing the load by the surface area of the indentation (H = P/A). The load varies from 1 to 120 kN.

Berkovich triangular pyramid-shaped diamond with a nominal angle 65.3° between the face and the vertical axis was developed as a sharper tip which manufacturing can comply with the ideal shape. These engineering approaches have been based on study of residual impression. The different scales of hardness were then established on the size of the impression.

The other approach was based on physical reasoning of measurements using theory of contact of different bodies, theory of plasticity or elastoplastic contacts. It enables to clarify the physical nature of behavior of different materials by indentation. The basic works on this idea were published by Archard, Bowden, Tabor, Sneddon and Loubet.

Both these approaches augmented by technical progress achieved a milestone consisting in a depth / displacement sensing indentation (DSI) technique. A typical test involves moving the indenter to the surface of the material and measuring the forces and displacements associated with the indentation process by continual recording of indentation depth vs. loading of the tip. It enables to derive many mechanical properties such as hardness, elastic modulus, strain energy (elastic, plastic, total), etc. from measured curves. In recent years, the study of mechanical properties of materials on the nanoscale has received much attention, as these properties can be size-dependent. These studies have been motivated partly by the development of nanocomposites and the application of very thin films for miniaturization of engineering and electronic components, and partly by newly available methods of probing mechanical properties in small volumes. The nanoindenter is maturing as an important tool for probing the local mechanical properties of materials.

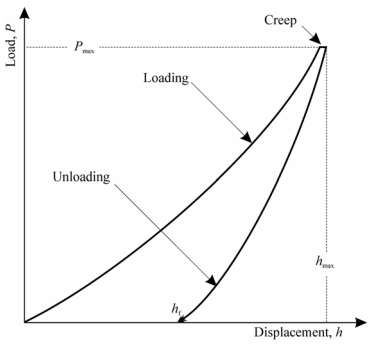

Fig. 1. **The typical DSI curve**

$$S = \frac{dP}{dh} = \frac{2}{\sqrt{\pi}} E_{\text{eff}} \sqrt{A} \qquad (1)$$

While originally derived for stiffness from theory of elastic contact for a conical indenter, it was established later that Eq. (*1*) holds equally well for spherical and cylindrical indenters and it may be applied to other geometries as well[1−3]. Here, A is the projected area of the elastic contact; E_{eff} is the effective elastic modulus

$$\frac{1}{E_{\text{eff}}} = \frac{1-\nu^2}{E} + \frac{1-\nu_i^2}{E_i} \qquad (2)$$

ν is Poisson's ratio, and i is label of indenter ($\nu_i = 0.07$, $E_i = 1141$ GPa for diamond). By measuring the initial unloading stiffness and assuming that the contact area is equal to the optically measured area of the hardness impression, the modulus can thus be derived from Eqs. (*1*) and (*2*). Stiffness $S = dP/dh$ is derived from the upper portion of the unloading data of DSI curve (Fig. 1).

The hardness is then calculated from its common definition:

$$H = \frac{P_{\max}}{A} \qquad (3)$$

where $P_{\max}$ is the peak indentation load and A is the projected area of the hardness impression. There are two approaches to calculation of H (programmed in software of different equipments). Doerner and Nix[4] suggested that the unloading stiffness can be computed from a linear fit of the upper one-third of the unloading curve. Point of intersection with axis of displacements they labeled as plastic depth h_{plast}. With knowledge of the indenter geometry, the plastic depth can then be used to obtain the projected area in contact with the indenter. If the final depth rather than the plastic depth is used, a significant overestimate of the hardness will result due to the significant decrease in depth during elastic recovery. If the Vicker's pyramid is used, the projected area is 24.5 $(h_{\text{plast}})^2$. Hardness is accordingly marked as H_{plast} and calculated from $P_{\max}$. Oliver and Pharr[5] published more precise and sophisticated method of analyse of unloading part of DSI curves. They reveal that unloading curves can be accurately described by the power law relation

$$P = \alpha (h - h_{\text{f}})^{\text{m}} \qquad (4)$$

where $(h - h_{\text{f}})$ is elastic displacement (elastic recovery is taken into account), and α, m are material constants. It is assumed that projected contact area at peak load is a function of the contact depth h_{c}, $A = F(h_{\text{c}})$. The functional form of F must be established experimentally prior to analysis – by calibration, e.g. The function is proposed in polynomial form with 9 terms which approach non-ideal shape of indenter.

Resolutions of such nano-equipments are in level of tithes of nm for displacements and in μN for loadings. Common loadings are in range of tens or hundreds mN and velocities in nm s^{-1}.

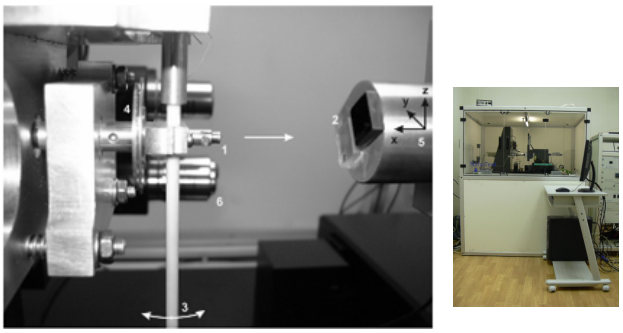

Fig. 2. **General view and measuring node of NT600:** 1 – indenter, 2 – samples, 3 – pendulum, 4 – capacitor plates, 5 – sample holder (x-y-z directions of moving), 6 – microscope

Measurements of hardness on bulk materials (steels) are correlated with stress investigation by X-ray diffraction (XRD), nanoindentations of plasma spray coatings and thin carbon based sputtered films. Thereinafter are briefly mentioned possibilities of utilization of nanotest devices.

2. Experimental device

Nanotester NanoTest™ NT600 (Micro Materials, Ltd.) was applied for all below mentioned experiments, Fig. 2. Details and accessories are described elswhere[6].

3. Utilisation

The nanotester NanoTest™ NT600 is fated to nanoindentations first of all. The set of analyzed samples was prepared from five *Fe alloys*[7,8]: carbon ferrite steel ČSN 12 050 (A), Mn-Cr steel 14 220 (B), Cr-Mo corrosion-resistant steel 17 135 (C), low-alloyed tool steel 19 313 (D), and Mo-W-Co rapid steel 19 852 (E). XRD stress analysis was performed on a Siemens goniometer with CrKα radiation. Macroscopic and microscopic lattice strains were evaluated from the α-Fe {211} diffraction line detected for nine tilt angles ψ ($\sin^2\psi = 0$, 0.1, 0.2, …, 0.8). The X-ray elastic constants $½s_2 = 5.76 \cdot 10^{-6}$ MPa^{-1}, $-s_1 = 1.25 \cdot 10^{-6}$ MPa^{-1} were used in stress calculations. Fig. 3 shows a strong correlation between surface microscopic stresses and hardness.

Investigation on metallographic polished cross section of plasma sprayed conventional titania (TiO_2) coating[9] revealed bimodal distribution of hardness – see histogram, Fig. 4. One maximum is at 11.9 GPa and the second one at 7.6 GPa. Plasma sprayed TiO_2 coating using conventional powder exhibits microhardness of about 8.5 GPa. The bimodal character is attributed to the presence of two different phases in the deposit.

Nanoindentations on DLC thin films (few μm) depos-

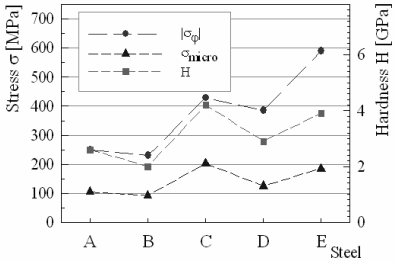

Fig. 3. **Surface compressive macroscopic stresses $|\sigma_\varphi|$, microscopic stresses σ_{micro}, (XRD) and the hardness *H* (DSI) for 5 batches of steel**

ited by magnetron sputtering on steel substrates. All the films are amorphous.

Structure of films with presence of hydrogen tends to polymer behaviour (very low hardness, strong influence of substrate on elastic modulus), Fig. 5. While elastic modulus for all presented films shows significant differences from substrate one and tends to some value of interlayer, the hardness tends to the substrate one.

Indentations of microscopic subjects such as crystals of zeolites

The local mechanical properties of columnar silicalite-1 crystals of a roof-prism shape with dimensions in μm of approx. 220 × 40 × 40 were investigated in state as-synthesized as well as calcined ones (i.e., crystals free of organic template), Fig. 6. Calcination was performed by heating (550 °C) these crystals in a dry-air stream for 24 hours. In fact, these crystals are porous twins with zigzag channels having their pore mouth openings on all four lateral faces[10].

Hardness of as-synthesized crystals, calcined crystals and fused silica bulk was compared. All silicalite-1 crystal twins have roughly the same elastic modulus (i.e., about 38 GPa), which is greater than one half of value for fused silica (71.6 GPa). Calcined crystals appear to be about twice harder (4.0 GPa) than as-synthesized ones (2.4 GPa) but they are about twice softer than fused silica (8.6 GPa)[11].

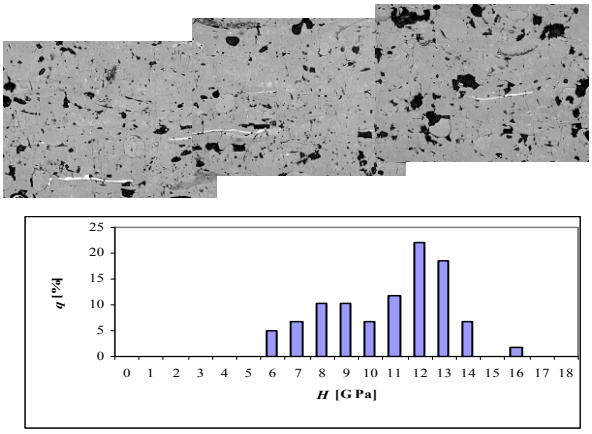

Fig. 4. **Histogram of hardness from 100 indents scattering a cross-section of TiO_2 coating**

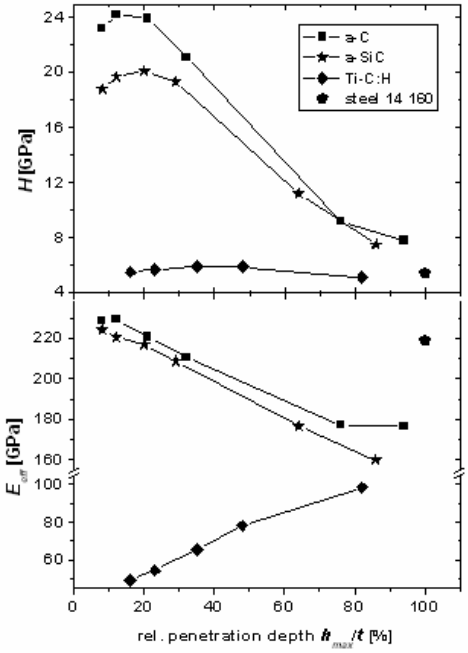

Fig. 5. **Depth profiles of hardness and elastic modulus in DLC films sputtered on the manganese-chromium steel CSN 14 160**

Nanocompression/nanoindentation experiments were performed on samples consisting of a sandwich composed of a Si substrate, an intermediate W-based film, and the investigated Al–Cu film. For nanocompression experiments were from these samples prepared cylindrical pillar with a diameter of 1.3 μm (height/diameter ratio of the pillar equal to 1.6) and to remove the Al and W films around the pillar by focused ion beam (FIB) milling, Fig. 7. The diameter of the removed zone was chosen to be 25 μm, to ensure that the operating punch will not touch

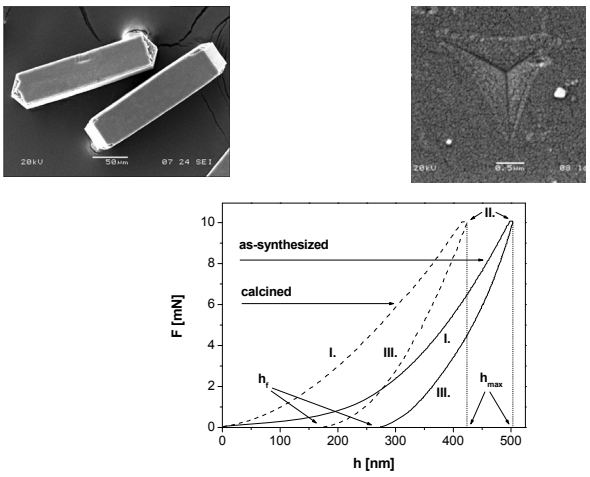

Fig. 6. **SEM image of silicalite-1 crystals (400x),residual impression into crystal, and the typical DSI curves for as-synthesized and calcined crystals**

any other object except the pillar. The conical diamond punch was used for all compression experiments. Its flat contact face had an irregular, approximately circular section of diameter of about 10 μm. The relatively large diameter of the flat punch face compared to pillar diameter ensured that despite a slight aiming misalignment, the selected pillars were always uniformly uniaxially deformed. It was also checked that the upper face of deformed pillars remained flat after the compression suggesting that it was completely covered with the flat tip. The nanocompression test was complemented with standard Berkovich tip nanondentation, which enables one to measure independently elastic properties and to correct the nanocompression stress–strain curve from parasitic elastic strains. Such a procedure thus provides a useful tool for the mechanical testing of thin films in condition of homogeneous stress state with improved precision of the stress–strain data[12].

4. Conclusions

Since beginning of the 20th century when Brinell first impressed his ball into the surface of the test specimen to differ various materials, especially different batches of steel, and theorists began investigate fields of strains and stresses under contact of two bodies, the technical progress enables to converge both these approaches. Sophisticated devices are able to determine not only hardness but due to analyses of DSI curve also elastic modulus and other mechanical properties in very small volumes.

There are briefly presented applications of the nanotester to indentations of bulk materials as well as thin films in this contribution. Investigation of local mechanical properties on specimens of microscopic sizes is referred as well. The nanotester with flat punch was used also for nanocompressions of micropillars prepared from thin film. All mentioned items represent stable/quasi stable measurements and were performed and published by authors. Moreover, various accessories for dynamic testing can extend spectrum of applications (adhesion, scratch and tribology tests, impact test, etc.).

Nanotesters are able to verify validation of laws of continuum mechanics for small volumes of materials as well.

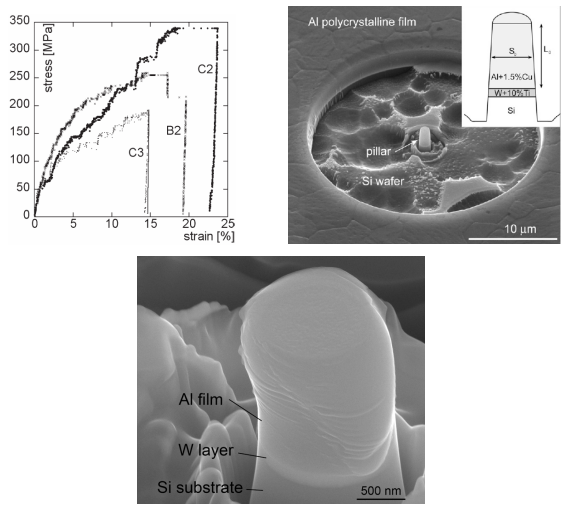

Fig. 7. **SEM pictures of pillar C2 before (rihgt) and after (below) nano-compression and stress – strain curves for different pillars**

Financial support from the Academy of Sciences of the Czech Republic: project KAN301370701, grant No. KJB201240701, and from Grant Agency of the Czech Republic project No. 106/07/0805 is acknowledged.

REFERENCES

1. Bulychev S. I, Alekhin V. P., Shorshorov M. Kh., Ternovskii A. P., Shnyrev G. D.: Zavod. Lab. *41*, 1137 (1975).
2. Pharr G. M, Oliver W. C., Brotzen F. R.: J. Mater. Res. *7*, 613 (1992).
3. King R. B.: Int. J. Solids Structures *3*, 1657 (1987).
4. Doerner M. F., Nix W. D.: J. Mater. Res. *1*, 601 (1986).
5. Oliver W. C., Pharr G. M.: J. Mater. Res. *7*, 1564 (1992).
6. Čtvrtlík R., Stranyánek M., Boháč P., Jastrabík L.: Mater. Struct. *13*, 90 (2006).
7. Ganev N., Čerňanský M., Boháč P., Drahokoupil J., Čtvrtlík R., Stranyánek M: *Proc. 22nd Danubia – Adria Sympos. Exp. Meth. In Solid Mech., Parma, Italy, Sept. 28 – Oct. 1, 2005*, 38.
8. Drahokoupil J., Ganev N., Čerňanský M., Boháč P., Čtvrtlík R., Stranyánek M: Z. Kristallogr. Suppl. *27*, 89 (2008).
9. Ctibor P., Bohac P., Stranyanek M., Ctvrtlik R: J. Eur. Ceram. Soc. *26*, 3509 (2006).
10. Caro J., Noack M., Richter-Mendau J., Marlow F., Petesohn D., Griepentrog M., Kornatowski J.: J. Phys. Chem. *97*, 13685 (1993).
11. Brabec L., Boháč P., Stranyánek M., Čtvrtlík R., Kočiřík M.: Micropor. Mesopor. Mat. *94*, 226 (2006).
12. Kruml T., Stranyanek M., Ctvrtlik R., Bohac P., Vystavel T., Panek P.: J. Mater. Res. *24*, 1353 (2009).

P. Bohac[a], R. Ctvrtlik[b], and M. Stranyanek[a]
([a] Institute of Physics, AS CR, v.v.i, Prague, Czech Republic, [b] Joint Laboratory of Optics, Palacky University and Institute of Physics AS CR, Olomouc, Czech Republic):
Potential Utilisation for Nanotesters

There are briefly presented applications of the nanotester to indentations of bulk materials as well as thin films in this contribution. Investigation of local mechanical properties on specimens of microscopic sizes is referred as well. The nanotester with flat punch was used also for nanocompressions of micropillars prepared from thin film. All mentioned items represent stable/quasi stable measurements and were performed and published by authors.

USE OF GENETIC ALGORITHM FOR IDENTIFICATION OF NONLINEAR CONSTITUTIVE MATERIAL MODELS

JAN BRUMEK*, BOHUMÍR STRNADEL, and IVO DLOUHÝ

VŠB – TU Ostrava, 17. listopadu 15, Ostrava
jan.brumek@vsb.cz

Keywords: Instrumented indentation test, material model, genetic algorithm

1. Introduction

Instrumented indentation is experimental method, which enables estimation of the values of mechanical properties from the record of dependence of indenter penetration depth on applied force. This method is especially suitable for construction materials, such as steel, if small dimensions of the specimen do not allow the use of conventional mechanical testing methods.

The instrumented indentation test used in this case is based on the well known Brinell's hardness test. Equipment of testing machines with a system for accurate recording of force and indenter penetration depth has enabled the development of methods for estimation of mechanical properties[1], such as elastic modulus, yield stress and strain hardening exponent. The Automated Ball Indentation Test[2] (ABI) is among the most widely used evaluation instruments. Due to repetitive indentation of spherical indenter into one spot, estimation of real stress and deformation can be realized. Typical process of an indentation test with the use of spherical indenter (Fig. 1) consists of loading part and unloading part.

Elastic modulus (3) is determined from the unloading phase of indentation test (Fig. 2). The value of elastic modulus is directly proportional to unloading curve slope.

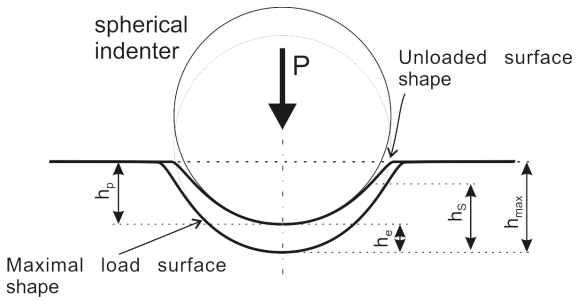

Fig. 1. **Indent imprint – cross section**

$$H = \frac{P_{\max}}{A} \tag{1}$$

$$E_r = \frac{\sqrt{\pi}}{2\sqrt{A}} \frac{dP}{dh} \tag{2}$$

$$\frac{1}{E_r} = \frac{1-\nu_m^2}{E_m} + \frac{1-\nu_i^2}{E_i} \tag{3}$$

$P_{\max}$ is the maximal loading force, E_m and E_i are the elastic moduli of the tested material and indenter tip, and E_r is reduced indentation modulus.

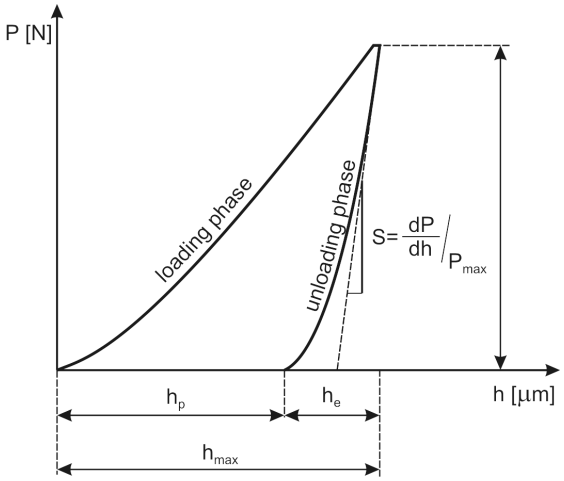

Fig. 2. **Force - displacement indentation curve**

Development of numerical modelling methods enables their use for the estimation of parameters in material models. The material properties estimation is based on searching for the minimum of function, which expresses the difference between a measured and a calculated process of indentation test. Non-linear material model in the finite element method is used for the analysis of a contact problem.

2. Finite element model description

For target function evaluation it is necessary to determine the indentation dependence by means of a numerical model. The indentation test is solved as a quasi-static axisymmetric problem with a non-linear material model. Finite element model assumes that a rigid spherical indenter is loaded with a normal force P and penetrates into the surface of an axisymmetric homogenous specimen occu-

pying the domain Ω {0, 2π} (Fig. 3). Uniaxial quasi-static indentation process is simulated by monotonically increasing the value ($h > 0$) of the penetration depth.

Another condition is that this process runs without any additional moments and friction. As this is a symmetric problem, a consequential axisymmetric contact problem is modelled for penetration depth $h = \{0; h_{\max}\}$. The indentation is modelled by the following contact problem finding the displacement field u(x,y) = (u1(x,y), u2(x,y)) in the solution of the unilateral problem:

(4)

$$\begin{cases} -\frac{\delta}{\delta x}(x\sigma_{11}(u)) - \frac{\delta}{\delta y}(x\sigma_{12}(u)) + \sigma_{33}(u) = 0, \\ -\frac{\delta}{\delta x}(x\sigma_{12}(u)) - \frac{\delta}{\delta y}(x\sigma_{22}(u)) = 0, \quad (x,y) \in \Omega \subset R^2; \end{cases}$$

The contact condition is:

$$\begin{cases} u_2(x,y) \le -h + \varphi(x), \sigma_{22}(u) \le 0, \\ [u_2(x,y) + h - \varphi(x)]\sigma_{22}(u) = 0, \\ \sigma_{12}(u) = 0, (x,y) \in \Gamma_0; \end{cases} \quad (5)$$

and boundary condition are defined:

$$\sigma_{11}(u) = 0, \sigma_{12}(u) = 0, (x,y) \in \Gamma_\sigma \quad (6)$$

$$u_1(0,y) = 0, \sigma_{12}(u) = 0, (x,y) \in \Gamma_1 \quad (7)$$

$$\sigma_{12}(u) = 0, u_2(x,0) = 0, (x,y) \in \Gamma_u \quad (8)$$

Where

$$\Omega = \{(x,y) \in R^2 : 0 < x < l_x, 0 < y < l_y\}, \quad l_x, l_y > 0$$

$$\Gamma_\sigma = \{(l_x, y) : 0 < y < l_y\}\} \quad \Gamma_0 = \{(x, l_y) : 0 \le x \le l_x\}$$

$$\Gamma_1 = \{(0,y) : 0 < y < l_y \quad \Gamma_u = \{(x,0) : 0 \le x \le l_x\}$$

and $\varphi(x) = \sqrt{R^2 - x^2}$ is a function of the curve of the spherical indenter with the radius *R*.

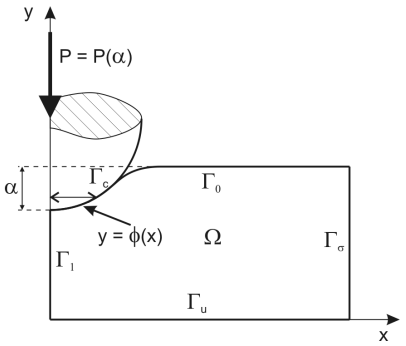

Fig. 3. **Geometry of the indentation problem**

Non-linear constitutive model (Fig. 4) used in analysis is:

$$\sigma = \sigma_y + C_1\varepsilon_{\text{pl}} + \gamma(1 - e^{-C_2\varepsilon_{\text{pl}}}) \quad (9)$$

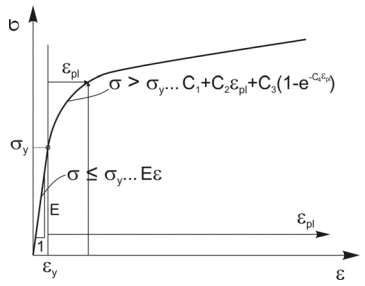

Fig. 4. **Constitutive model for material non-linearity**

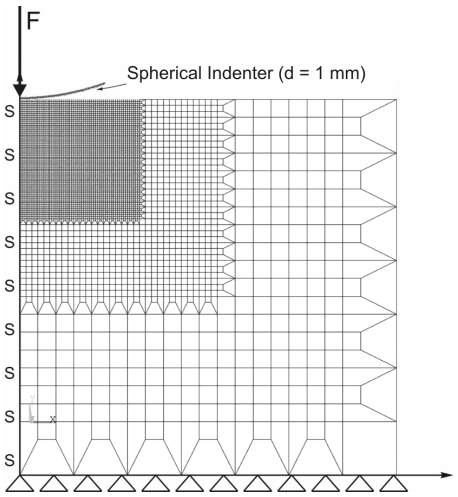

Fig. 5. **Finite element mesh**

3. Optimization algorithm

An optimization method using a genetic algorithm is utilized for the location of the target function minimum. Target function is composed of the measured indentation curve and indentation dependence calculated with a finite element model. The form of the target function proposed for this model:

$$F(X_1, X_j, ...X_m) = \sum_{i=1}^{n} \sqrt{\left(Y_i - Y_i'\right)^2} \quad (10)$$

The genetic algorithms start with randomly chosen parent chromosomes from the search space to create a population. They work with chromosome genotype. The population "evolves" towards the better chromosomes by applying genetic operators modelling the genetic processes occurring in the natural selection, recombination and mutation. The selection compares the chromosomes in the population aiming to choose these, which will take part in

the reproduction process. The selection occurs with a given probability on the basis of fitness functions. The fitness function plays a role of the environment to distinguish between good and bad solutions. The recombination is carried out after selection process is finished. It combines, with predefined probability, the features of two selected parent chromosomes forming similar children. After recombination offspring undergoes mutation. Generally, the mutation refers to the creation of a new chromosome from one and only one individual with predefined probability. After three operators are carried, the offspring is inserted into the population, replacing the parent chromosomes from which they were derived, producing a new generation. This cycle is performed until the optimization criterion is met (Fig. 6).

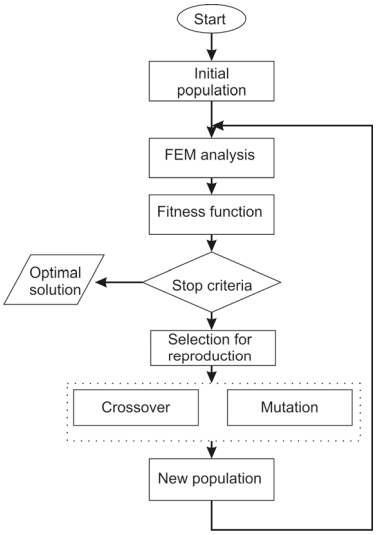

Fig. 6. **Flow diagram of genetic algorithm**

4. Experiment

For verification of the proposed method a set of steels was selected, on which experimental measurements were realized. The materials are listed in Table I. The experiment was processed with constant speed of loading. Samples surfaces were polished before the experiment until a mirror gloss was achieved.

Table I
Specimens' microstructure characterization

Mark	Micro-structure
R7T	Ferrite + pearlite
34CrMo	Bainite
CrMoV	Bainite
11375	Ferrite + pearlite

5. Discussion and results

Material model parameters for steel samples are estimated on the basis of the proposed method and experimental test. The results of the analysis are summarized in Table II. Values of yield stress and ultimate tensile stress from uniaxial tensile test are given in the right part of the table.

Table II

Mark	σ_y	C_1	γ	C_2	Re
R7T	532	345	419	27,8	552
34CrMo	1032	116	134	16,2	1053
CrMoV	682	151	203	33.2	708
11375	232	453	202	26,2	252

The final processes of a single materials indentation curve are depicted and compared with loading parts processes calculated with numerical model (Fig. 7).

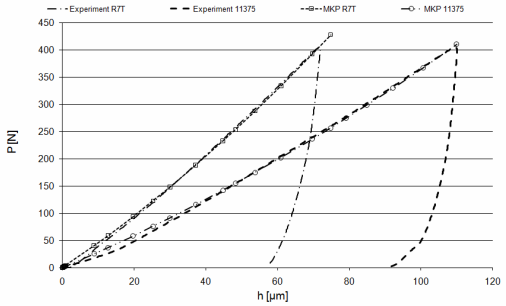

Fig. 7. **Indentation curves comparison** (R7T and 11375 samples)

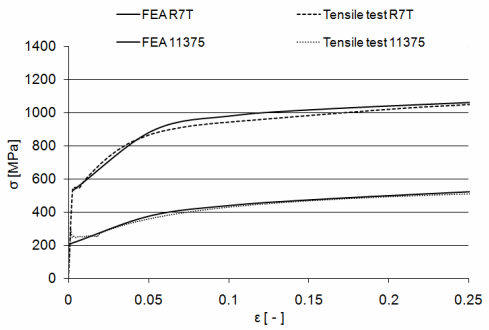

Fig. 8. **Comparison of the material model and tensile test curve** (R7T and 11375 samples, plotted in true stress-strain values)

6. Conclusion

The proposed method for the estimation of mechanical properties by instrumented indentation was verified on a set of construction materials. Optimization algorithm for searching of minimum of target function through evolution techniques was proposed. This system accomplished a reduction of the number of iteration steps in the process of searching for optimal solution. The results reached with the proposed method were compared to a true stress and true strain curve process from uniaxial tensile test. Results of predicted properties are in good correspondence.

The work was supported by Ministry of Industry and Trade of Czech Republic no. 2A-TP1/023.

REFERENCES

1. Oliver W. C., Pharr G. M.: J. Mater. Res. *7*, 1564 (1992).
2. Taljat B., Zacharia T.: Int. J. Solids Structures *35*, 4411 (1998).
3. Haggag F. M., Nanstad R. K., Braski D. N., in: *Innovative Approaches to Irradiation Damage and Fracture Analysis* (Mariott D. L., Mager T. R., Bamford W. H., ed.), vol. 170, pp. 101−107. ASME PVP, 1989.

J. Brumek, B. Strnadel, and I. Dlouhý *(VŠB – TU Ostrava):* **Use of Genetic Algorithm for Identification of Nonlinear Constitutive Material**

Indentation technique was focused on the prediction of the strain hardening behaviour of carbide steels. An improved technique to determine the plastic properties of material from the load-displacement curve from a ball indentation test was proposed. The time needed for finding an optimal solution for a non-linear constitutive model depends on a number of design variables. Common methods like gradient methods or linear programming can fail due the fact that they drop to the local minimum. The advantage of a genetic algorithm is that it does not require the knowledge of target function. Proposed method was applied to the data from the instrumented indentation technique. The results were found to be in good agreement with the data from conventional standard tests, and in less time.

APPLICATION OF THE SURFACE ROUGHNESS SPECTRUM ANALYSIS AT DIAGNOSING FUNCTIONAL PERFORMANCE OF ARMAMENT COMPONENTS

RENATA DVOŘÁKOVÁ*, EMIL SVOBODA, and KAREL MAŇAS

Department of Mechanical Engineering, University of Defence Brno, Kounicova 65, 66210 Brno
renata.dvorakova@unob.cz

Keywords: properties, surface, surface texture, roughness, power spectral density, frequency spectrum

1. Introduction

The performance of surface layers in various components can be strongly influenced by the character of load in operation. Another important factor, which should be investigated, is the micro-topology of contacting surfaces. Standard characteristics: Ra, Rq, Rt, Rsk, Rku, or RΔq, Rsm are largely applied to measure and quantify the surface texture. But these classic parameters are rather limited and inadequate to decide proper methods of machining, assessing functional properties of the surface or characteristics of the machine tool.

Integral methods based on the statistic, correlation and frequency analyses are not used in the meantime. Advantage of the statistic characteristics is in describing profiles or areas of the surface by minimum number of parameters, incorporating not only the peak to valley heights, but also the frequency and profiles in the surface.

The article describes the application of an integral method in the surface assessment to examine changes in a specimen surface at a fatigue test, using the acquired data to predict functional performance of components, namely the functional performance of the barrel bore top end.

The article's aim is to evaluate the relation between the surface quality and its functional performance by unconventional and non-standard characteristics.

2. The Surface Texture Characteristics

Prospective of the surface texture integral characteristics appear: autocorrelation function and power spectral density, and the related frequency spectrum of the profile. They may become powerful diagnostic tools capable of revealing e.g. slight changes in the surface texture produced by the cutting tool, undetectable by the classic parameters, or changes in the surface texture functional performance, seeming to be small by the classic parameters.

Autocorrelation function (ACF) can evaluate periodicity or randomness in surface profile features. The autocorrelation function can be used to evaluate surface condition, e.g. the zero points or disintegration of autocorrelation function, to calculate the index of plasticity at analysing rate and/or character of deformations in the surface projections. The autocorrelation can distinguish randomness from periodicity within a signal, i.e. to differentiate random and periodic processes. Besides, it enables to reveal a periodicity component in a mix with random components.

Power spectral density (PSD) function allows analysing surface profile density components by the individual frequencies. The function records the maximum value of the basic component profile; but there are other harmonic components, expressed as multiples of primary density. It describes variations in the inspected surface, both in terms of frequency (peak to valley spacing) or spectral density wavelengths, and their amplitude (magnitude). Higher spectrum density and volume involve higher number of harmonics and their magnitude. To analyse the surface spectral density, use may be made e.g. of the wavelength corresponding to the most recurring frequency (100% value).

The function can be applied in practice, e.g. at textured surface analysis, namely when a tiny change in size is found out in the classic roughness parameters (Ra, Rz etc.), but resulting in roughness change (often even markedly) of the analysed surface both in the frequency (variations in the surface texture spacing) or in the wavelength variations and their amplitudes.

In the graphics, the vertical axis shows the power spectral density in μm^2, i.e. the amplitude area A^2. The vertical axis shows the wavelengths λ [μm] ($\lambda = 1/f$). There are dominant wavelengths seen in the graphics. Their amplitude equals the square root of the corresponding value on the vertical axis.

Frequency spectrum of the profile (FS) implies frequencies of the range given by their wavelengths to ease their identification. The height of the spectrum line indicates the power (force) of a period in the profile. Spectral analysis allows to set-up the periodicity and orientation of a phenomenon that exists along with the roughness, namely by means of a frequency picked from the spectrum. If the profile involves a periodic phenomenon, then the frequency spectrum line (or a series of lines) will step high.

In the graphics, the wave number of spectral lines is plotted on the horizontal axis. The first spectral line corresponds to the profile length L; the second spectral line corresponds to L/2, third to L/3 etc. Thus e.g. the spectral line of λ (12) = 4/12 = 0.333 [mm] for the profile of the length of 4 mm (see Table I on the left, 4th row) corresponds to 12, the spectral line of the wave-

length λ (12) = 4/12 = 0.333 [mm]. The spectral lines in the left part of the spectrum correspond to long wavelengths (i.e. to low frequency); the spectral lines in the spectrum right part correspond to short wavelengths (i.e. to high frequencies).

The graphic's vertical axis presents amplitudes of the relevant wavelengths, i.e. the signal power or intensity of the relevant frequency. The wave number with dominant magnitude (amplitude) is highlighted.

3. Fatigue of Materials

Fatigue of materials is a serious problem – affecting 90% of engineering components and structures. It develops in components under cyclic load, to crack at stresses much lower than their material strength and yield point proved in their static test.

Hence, a fatigue crack is the most frequent cause of component failures, initiating new surfaces. It develops from cyclic loads, totally restructuring the dislocation field, redistributing dislocations in the loaded material, splitting up the almost defect-free metallic matrix, with multivariate internal interface lines, into the so-called mosaic blocks. The dislocations are mostly concentrated into certain zones (e.g. interface lines of the mosaic blocks), whereas the greater part of matrix volume has few dislocations. This irregularity increases with the number of fatigue cycles, causing dislocations to amass increasingly on mosaic block interfaces, whereat the micro cracks grow. In other words, the fatigue localizes the deformation, making its distribution irregular. This is the reason why the cyclic loaded components can bear much lower load (amplitude) than is their static strength.

Repeated changes in the fatigue load cause the irregularities to intensify the dislocation distribution and more intensive interactions among them. Gradually, they develop into a "wall" that becomes impenetrable for the dislocations in motion. Such "walls" then segment the crystal into blocks, with only few dislocations to remain. Although they are movable, their movement is limited by the boundaries of the mosaic block. The dislocation density then intensifies along those boundaries.

Outwardly, these material structure changes will grow exactly in the surface texture changes in form of surface roughness or waviness.

4. Application of the Surface Texture Integral Characteristics

Two unconventional characteristics were applied to assess the surface texture changes of the specimens, namely the power spectral density (PSD) and the frequency spectrum (FS), added up for illustration with amplitude distribution (density) and material ratio curve. These tests were carried out at pure bending of flat specimens. The experiments proved that significant changes occurred in the surface texture during the tests. These changes were gauged by the contact confocal gauge Talysurf CLI 1000 to check roughness, assessed by the above described characteristics, and compared against the standard parameters.

Table I shows specimen surface roughness profiles before and after the fatigue test with the usually applied Ra parameter (mean arithmetic deviation of the assessed profile within the basic interval). The growth of Ra value by 1.85 is evident. Also evident after the test are extreme valleys and peaks that cause huge growth of roughness Rt profile height. The second row in Table I showed the amplitude density curves (grey histogram), and material ratio curves of the profile. Well visible here are the changes in the amplitude on the surface texture before and after the test, in the direction of amplitude spectrum distribution width narrowing against a major rise of the amplitude.

The third row in Table I showed the comparison of the power spectrum densities. Apparent are here the changes in the surface texture before and after the test. They are actually changes both in the relief division, but mainly in the area size under the PSD curve. The major differences are at wavelengths λ = 0.8–1.4 mm, when the PSD value increases approx 10 times. The fourth row in the Table is an additional assessment, presenting the profile of frequency spectra. There are visible changes in the single wave numbers, whereat a transformation occurs from the wave numbers 4–15 with the dominant wave number 12 (on the profile before fatigue test) into two dominant wave numbers (4 and 5), with the doubled amplitude.

The fatigue test results were used to assess functional performance changes of the rifled bore surface texture. The rifled surface texture was assessed in the course of the barrel performance, always after 1,000 gunshots. The initial value represented the rifled surface texture of a new barrel. The surface roughness profile of the new barrel rifles was uniform, while after 5 thousand gunshots it has shown removal of the unevenness peaks as a result of wear, with major valleys (of stratified nature). Also the division of amplitudes and material ratio corresponded to this state. The firing barrel standard parameter Ra average growth was 15%.

Different results were attained in the assessment by PSD (and FS) parameter. Figs. 1 and 2 show that significant changes occurred in the surface texture during the barrel performance. Fig. 1 shows comparison of the power spectral density for the new barrel (hatched area) and for the fired barrel (white area). This, so far not normalized parameter, shows a major increase of values in the area of the wavelengths λ = 0.286–0.105 mm, namely more than 3.5 times. There can be detected three dominant wavelength areas, namely for λ ≈ 0.2 mm, λ ≈ 0.5 mm, λ ≈ 0.8 mm. These three dominant wavelength areas increased their power spectra by 1.5 up to 3.6 times, not so evident with the other wavelengths (see Table II).

Table I
Review of Surface Roughness Characteristics for the Fatigue Test

Area roughness profile before the test

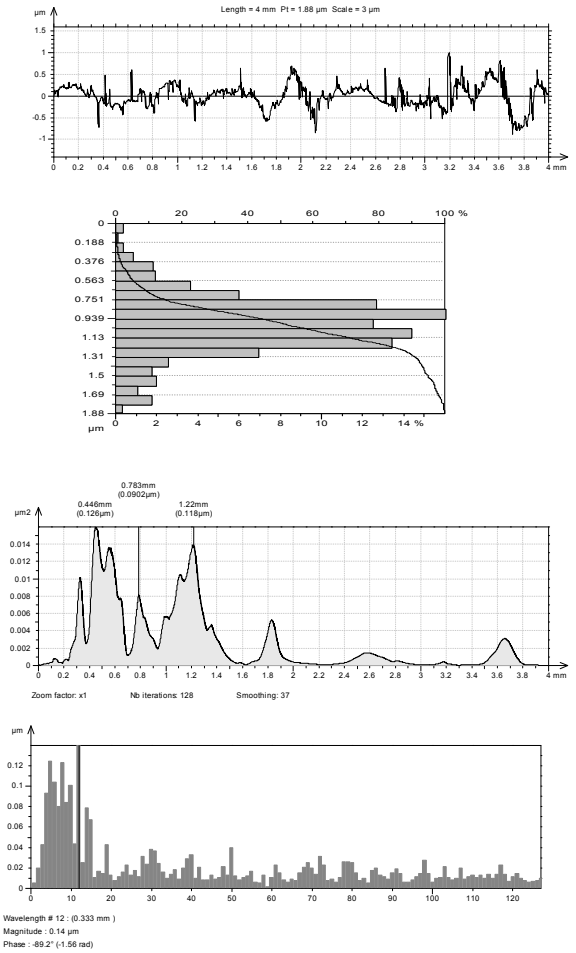

Area roughness profile after the test

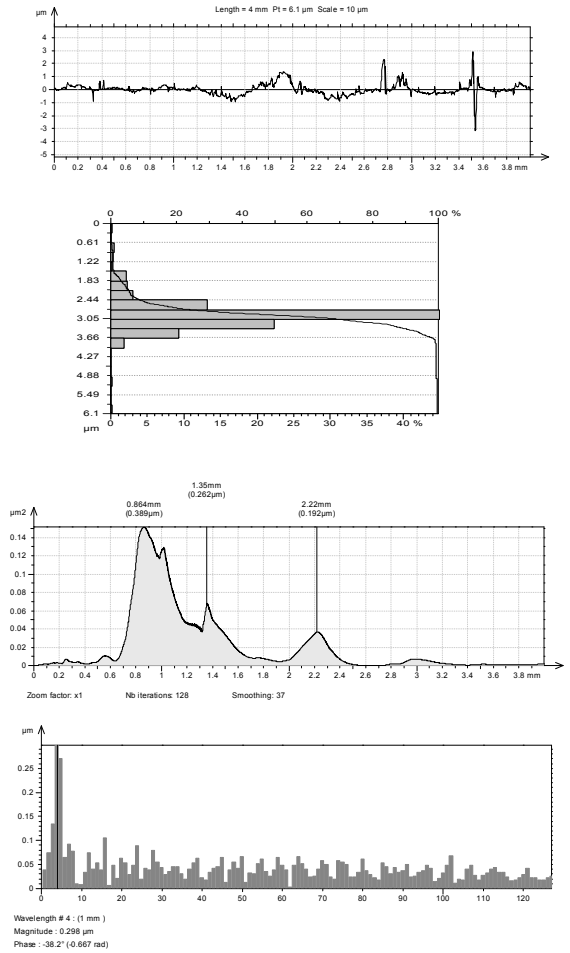

Table II
Review of the dominant wavelengths for a new barrel and a firing barrel

New barrel			Barrel after 5 000 shots		
λ [mm]	A [µm]	PSD [µm^2]	λ [mm]	A [µm]	PSD [µm^2]
0.111	0.030	0.012	0.111	0.299	0.017
0.222	0.050	0.015	0.222	0.210	0.055
0.800	0.180	0.035	0.800	0.230	0.045

Fig. 2 shows the frequency spectra for both barrels – black colour means wave numbers with their relevant amplitudes for the new barrel, while grey colour is for the firing barrel. Also here are evident changes with ampli-

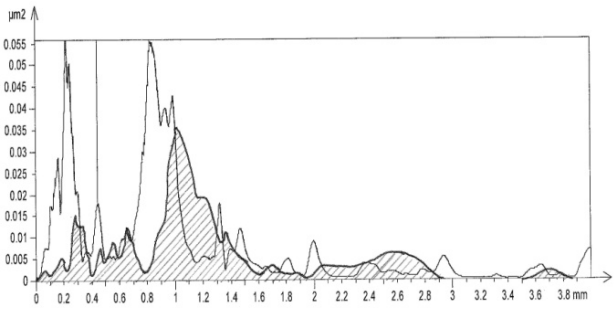

Fig. 1. **Comparing a new barrel PSD** (hatched area) **with a barrel after 5,000 gun shots** (white area)

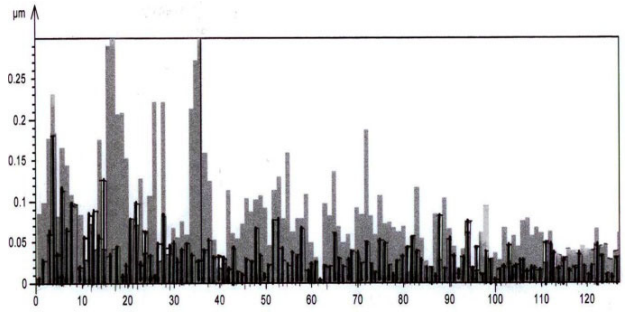

Fig. 2. **Comparing a new barrel FS** (black curves of wave number) **with a barrel after 5,000 gunshots** (grey curves)

tudes of single wave numbers. The largest amplitude increments are at the wave numbers (14 – 38), what corresponds to values λ = 0.286–0.105 mm given in Fig. 2 graphic chart. Another area with huge amplitude changes is for the wave numbers (2–6), what corresponds to values λ = 2.00–0.667 mm in Fig. 2 graphic chart. The amplitude value increments matching single wave numbers are even (10 up to 20) multiples.

Table II shows a review of dominant wavelength parameters for a new and a fired barrel. There are three dominant wavelengths chosen for both barrels described above, namely λ = 0.111 mm (wave number 36), λ = 0.222 mm (wave number 18), and λ = 0.800 mm (wave number 4). Data shown in the next column are amplitudes for these wavelengths readout from Fig. 2; the PSD value is readout from Fig. 1.

5. Conclusions

Advantage of the unconventional parameters is that they describe a profile or area primarily by frequency and shape parameters of the surface. These parameters can detect even small variations in the surface texture due to cutting tool, machine, or material, which are undetectable by the classic parameters.

This method is able to identify also changes in the surface texture performance, becoming evident in slight changes of the classic parameters, proved both in the measurement on the barrels mentioned herein, and in the measurement of surface roughness at the fatigue tests, i.e. with roughness altered to higher wavelengths (waviness).

Application of the unconventional parameters used in the assessment of the functional performance tends towards the processing of textured surfaces, i.e. the surfaces based on their own physical substance, and with features corresponding to the required functional performance (a "tailor-made" surface). Exactly these textured surfaces are normally characterized by the wavelength of profile roughness, statistic and spectral characteristics.

This contribution was sponsored by the research intent MO0FVT0000404 "Research and Development of Modern Materials and Technologies for the Military Equipment Applications" and the grant GA CZR 106/08/1243 "Research of the Plasma Nitriding of Internal Cavities".

REFERENCES

1. Whitehouse D. J.: *Handbook of Surface Metrology*, pp. 44 – 101, and 251–264. Institute of Physics Publishing Bristol and Philadelphia 1994.
2. Whitehouse D. J.: *Surfaces and their Measurement*, Kogan Page Science, 2004.
3. Novák Z.: Prostorové hodnocení textury povrchu (Spatial Assessment of the Surface Texture). *Studie*. Brno 2006.
4. ČSN EN ISO 4288 *Geometrical Product Specifications (GPS) – Surface Texture: Profile Method – Rules and Procedures for the Assessment of Surface Texture.* ČSNI 1999.
5. Fiala J., Kraus I.: *Povrchy a rozhraní* (Surface and Interface), pp. 108–152. ČVUT, Praha 2009.

R. Dvořáková, E. Svoboda, and K. Maňas *(University of Defence Brno)***: Application of the Surface Roughness Spectrum Analysis at Diagnosing Functional Performance of Armament Components**

The article describes the application of an integral method in the surface assessment to examine changes in a specimen surface at a fatigue test, using the acquired data to predict functional performance of components, namely the functional performance of the barrel bore top end. The article's aim is to evaluate the relation between the surface quality and its functional performance by unconventional and non-standard characteristics. Application of the unconventional parameters used in the assessment of the functional performance tends towards the processing of textured surfaces, i.e. the surfaces based on their own physical substance, and with features corresponding to the required functional performance. Exactly these textured surfaces are normally characterized by the wavelength of profile roughness, statistic and spectral characteristics.

EFFECT OF TIME ON NANOINDENTATION ELASTIC MODULUS OF THREE DIFFERENT DENTAL RESTORATIVE COMPOSITES

RENATA EICHLEROVÁ[a]*, JAROSLAV LUKEŠ[a], SVATAVA KONVIČKOVÁ[a], and PAVEL BRADNA[b]

[a] Laboratory of Biomechanics, Department of Mechanics, Biomechanics and Mechatronics, Faculty of Mechanical Engineering, Czech Technical University in Prague, Technická 4, 166 07 Prague 6, Czech Republic; [b] Institute of Dental Research, 1st Faculty of Medicine, Charles University, General Faculty Hospital in Prague, Karlovo náměstí 32,121 11 Prague 2, Czech Republic
eichlerova.renata@seznam.cz

Keywords: nanoindentation, restorative composites, elastic modulus, time dependency

1. Introduction

Filling composite materials are widely used in dentistry in the last 15 years for their aesthetic aspects, good biocompatibility and no toxicity. The reasons against use of amalgam alloys were aesthetic aspects, toxicity and environmental pollution by mercury waste. Lifetime of composite filling is satisfactory but there is still a need for improvement. Fractures of filling, secondary caries or loss of filling sometimes occur. Due to mechanisms such as occlusal loading and shrinkage of composites could create stresses in filling and adhesive layer and these stresses cause failures of the tooth-restoration interface and undermine marginal integrity[1]. The value of stress can be influenced by cavity shape and use of suitable materials. The problem could be solved through the minimizing of interfacial stress by optimizing the cavity shape using modern shape optimizing techniques. For stress analysis and design of cavity shape a finite element program are used[2]. Value of elastic modulus of resin-composite in performed analyses is considered to be constant in time. The intent of this study was to determine elastic modulus of different filling materials for the use in such analysis and to observe changes of mechanical properties in different time after polymerization. Due to better knowledge of material properties more accurate results of analyses could be reached.

2. Materials and Methods

Nanoindentation modulus of three different materials was tested in this study. First chosen material Filtek™ Silorane (3M ESPE, Dental Products, St. Paul, U.S.A.) is a visible-light activated, low-shrink restorative composite for posterior restorations. The main advantage of this composite is excellent marginal integrity and reduced risk of secondary caries due to lowest polymerization shrinkage (<1%). This low shrinkage significantly reduce polymerization stress thereby decrease the risk of enamel fractures and postoperative sensitivity. Filtek™ Silorane has excellent compressive strength for stress-bearing restorations and high flexural strength protecting the tooth from fractures. Second chosen material Filtek™ Supreme XT (3M ESPE, Dental Products, St. Paul, U.S.A.) is a visible-light activated, universal restorative composite designed for use in anterior and posterior restorations. This material is based on 3M ESPE`s nanotechnology, which combines excellent strength with low abrasion and polymerization shrinkage (<2,5%). Filtek™ Supreme XT contains bis-GMA, UDMA, TEGDMA, and bis-EMA resins. All shades except for the translucent shades are radiopaque. The fillers for the radiopaque shades are a combination of zirconia/silica and silica filler with an average primary particle size of 5-20 nm. Third chosen material Charisma (Heraeus Kulzer GmbH, Hanau, Germany) is microglass universal hybrid composite for posterior restorations. Charisma is based on bis-GMA matrix. The content of filler is 64% (by volume) and is combination of barium aluminium fluoride glass (0,02–2 microns) and highly dispersive siliciumdioxyde (0,02–0,07 microns). Charisma is light curing and radio-opaque composite with high strength and wear resistance provide long-lasting restorations. These materials represent different types of filling restorative composites used in dentistry nowadays.

Three disc specimens (4 mm in diameter and 2 mm in height) of each material were prepared in Teflon mould. Moulded material was covered from both sides by transparent plastic film and was pressed between two glass slides. Polymerization of material was activated by using of light curing unit (Translux Power Blue™, Hereaus Kulzer GmbH, Germany) for time period according to instructions for use. Each specimen was irradiated only from one side and this side was tested. After polymerization the specimen was finished mechanically in grinding machine with abrasive papers with subsequently decreasing abrasiveness up to 4000-grit and then was polished. Thus prepared specimen was stick on magnetic metal thin plate in order to prevent movement of specimen during indentation.

The nanoindentation testing was performed using a Hysitron's TriboLab® (Hysitron, Inc., Minneapolis, USA) at the CTU in Prague. System possess the option of *in-situ* SPM imaging, extended force transducer SN5-484-01, active vibration isolation and piezo automation with precision of the indent placement less then 0,1 μm. A Berkovich tip was a nanoindenter used for material

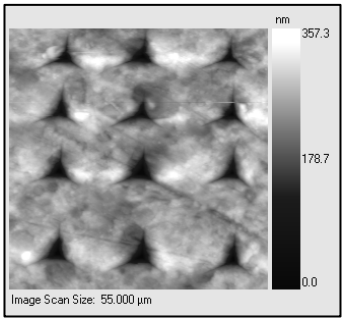

Fig. 1. **Detail of indentation area**

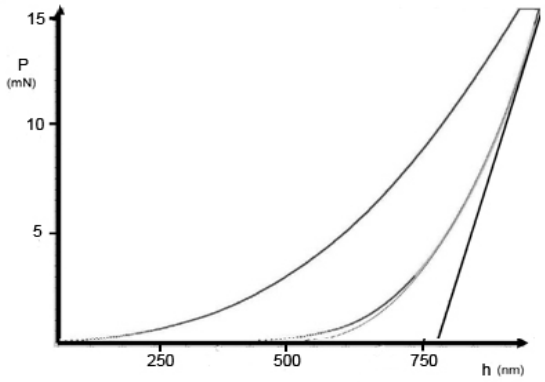

Fig. 2. **Typical load-displacement graph of the nanoindentation where the loading, holding and unloading segments are evident**

properties testing. A shape of the tip is a three sided pyramid with a total included angle of 142,3 degrees and a half angle of 65,35 degrees. The Berkovich tip has the same projected area to depth ratio as a Vickers indenter, but it is easier to grind this tip to a sharp point and so is more readily employed for nanoindentation type tests[3]. Load function of the load control testing cycle consisted of three segments: loading, holding at the peak of load and fully unloading. Each part of trapezoidal function lasted 10 seconds and maximum applied load was 15 mN. Twelve indentations were placed in matrix 3×4 about separation of 15×20 µm in order to avoid the mutual influence, as in Fig. 1. These indentations on randomly selected areas were performed on each specimen in every time of measurement.

The model chosen to interpret the indentation data were that of Oliver and Pharr[3]. Indentation elastic modulus E_r has the following relationship (*1*) with the elastic modulus of the material, namely:

$$\frac{1}{E_r} = \frac{\left(1-\nu^2\right)}{E} + \frac{\left(1-\nu_{tip}^2\right)}{E_{tip}} \qquad (1)$$

where E and ν are elastic modulus and Poisson's ratio of the sample, E_{tip} and ν_{tip} are elastic modulus and Poisson's ratio of the indenter, respectively[4,5]. Mentioned above elastic modulus and Poisson`s ratio of the indenter and indentation modulus must be known in order to determine the elastic modulus of the material. The elastic properties of the diamond Berkovich indenter are already known as: E_{tip} = 1141 GPa and ν_{tip} = 0,07 (ref.[6]). Poisson's ratio ν = 0,3 for resin-composites is used[4]. The indentation modulus is one of many material properties that can be gained from the load-displacement graph of the nanoindentation test (Fig. 2).

In order to observe effect of time on indentation modulus, different time intervals between nanoindentations of specimens were determined as follows: 1 hour, 1 day, 1 week and 1 month after specimen manufacturing. Specimens were stored in dark and dry place at room temperature all the time.

3. Results

The mean elastic moduli of all three tested materials are presented in Tab. I. The data were analyzed by analysis of variance and T-test. Statistically significant differences among the time groups at $P < 0,05$ revealed. Each tested material presented significant increase of elastic modulus between the first and the third time interval. For Filtek™ Supreme XT and Filtek™ Silorane, significant decrease of elastic modulus was observed between the third and the fourth time interval which was not the case of the Charisma.

Table I
Mean elastic moduli and variation coefficients of the resin-composite tested in different times after manufacturing of specimens

Time interval	Mean elastic modulus E [GPa] (variation coefficient [%])		
	Filtek™ Supreme XT	Filtek™ Silorane	Charisma
1 hour	13,1 (6,1)	11,9 (1,6)	5,8 (3,4)
1 day	14,2 (0,8)	12,4 (10,2)	6,4 (4,4)
1 week	17,6 (4,5)	14,2 (6,4)	7,8 (3,8)
1 month	12,5 (2,4)	10,8 (15,7)	8,0 (6,2)

4. Discussion

Poisson`s ratio of 0,3 was assumed for all materials. If the Poisson`s ratio of the material was different the calculated elastic modulus would decrease quadratically with increasing Poisson`s ratio[4]. No significant differences between the three specimens made of the same material and measured at the same time was found. Each tested material showed significant increase in modulus after 1 week

(standard deviation in parenthesis): Filtek™ Silorane (11,9 (0,2) – 14,2 (0,9)), Filtek™ Supreme XT (13,1 (0,8) – 17,6 (0,8)), Charisma (5,8 (0,2) – 7,8 (0,3)). Decrease of modulus occurred for both 3M ESPE materials after 1 month: Filtek™ Silorane (10,8 (1,7)), Filtek™ Supreme XT (12,5 (0,3)). Modulus of Charisma remained almost unchanged with small increase: Charisma (8,0 (0,5)). The highest modulus had Filtek™ Supreme and Charisma had lower modulus than Filtek™ Silorane. In parallel with this research, elastic moduli were examined also by the three-point bending test. The elastic moduli were lower in comparison with nanoindentation testing. Time set for the three-point bending test prescribed in ISO 4049:2000 is 24 hours after the specimen manufacturing. The results obtained by nanoindentation testing showed that the elastic modulus of resin-composites take different values in time and this effect could not be examined by three-point bending test. No standards for dental resin-composites nanoindentation testing are available at the moment.

5. Conclusions

Nanoindentation is an effective method for elastic modulus evaluation. Due to non-destructive character of this method in terms of possibility to measure one specimen in different areas more than once we can determine the effect of time on mechanical properties, namely on elastic modulus. The sample surface preparation is very important for obtaining correct results because the use of nanoindentation technique requires a very smooth and flat sample surface. Results from nanoindentation revealed that the time has a considerable effect on the development of elastic moduli of the tested samples. These changes can be explained by the setting reaction of polymer matrix and filling particles after polymerization. We conclude that elastic modulus of tested materials vary in time.

The research was supported by the Ministry of Education project: Transdisciplinary research in Biomedical Engineering II, No. MSM 6840770012 and Research Plan MSM 6840770003.

REFERENCES

1. Hickle R.: Eur. Ceram. Soc. *2008*, 7278.
2. Shi L., Fok A. S. L., Qualtroug A.: Dental Material, *24*, 1444 (2008).
3. Fischer-Cripps A. C.: *Nanoindentation*, Mechanical Engineering Series, 223 Spring Street, NY, 10013, USA: Springer Science+Business Media, LLC, 2nd ed., 2004.
4. Masouras K., Akhtar R., Watts D. C., Silikas N.: J. Mater. Sci.: Mater. Med. *19*, 3561 (2008).
5. He H. L., Swain M. V.: J. Dentistry *35*, 431 (2007).
6. Ziopus P., Rogers K. D.: J. Bionic Engineer. *3*, 019 (2006).

R. Eichlerová[a], J. Lukeš[a], S. Konvičková[a], and P. Bradna[b] *([a] Department of Mechanics, Biomechanics and Mechatronics, Faculty of Mechanical Engineering, Czech Technical University in Prague; [b] Institute of Dental Research, 1st Faculty of Medicine, Charles University, General Faculty Hospital in Prague)*: **Effect of Time on Nanoindentation Elastic Modulus of Three Different Dental Restorative Composites**

The intention of this study was to determine elastic modulus of different resin-composite filling materials for the use in FEM analyses and to observe changes of mechanical properties in different time after polymerization. Nanoindentation was chosen as suitable non-destructive method for elastic modulus determinations. Each tested material presented changes in modulus in dependence on time after specimens moulding. We conclude that elastic modulus of tested materials vary in time. These changes can be explained by the setting reaction of polymer matrix and filling particles after polymerization.

DETERMINING THE TRUE STRESS-STRAIN RELATIONSHIP BY DEPTH SENSING INDENTATION ON TWO STRUCTURAL MATERIALS

PETRA GAVENDOVÁ[a], PAVOL ZUBKO[b], LADISLAV PEŠEK*[b], and OLGA BLÁHOVÁ[c]

[a] Institute of Materials Research, Slovak Academy of Sciences, 043 53 Košice, Slovakia, [b] Department of Materials Science, Technical University of Košice, Faculty of Metallurgy, 042 00 Košice, Slovakia, [c] New Technologies-Research Centre, University of West Bohemia, Univerzitní 8, 306 14 Plzeň, Czech Republic
petgav@post.sk

Keywords: Depth Sensing Indentation, spherical indentation, stress-strain curve

1. Introduction

The increasing need for evaluation of the mechanical properties of small volumes of materials caused rapid development in depth sensing indentation technique (DSI) over the last decade. Loading force, F, and indentation depth, h, are continuously recorded during the loading and unloading cycle. In DSI, the test result is an indentation curve[1]. However, sharp indenter does not enable one to measure various deformation states, a spherical indenter has been used more often for this purpose. A sphere has the advantage that the effective strain changes as a function of indentation depth. Thus, wide range of indentation strains can be obtained with the increasing force at the same spot without changing the indenter[2]. Therefore, the stress – strain, σ – ε, curve can be determined by spherical indentation. The mean contact pressure differs in different stages of the ball indentation[3]. For the initial elastic regime, the mean contact pressure (p_m) increases linearly with the square root of the indentation load. When p_m reaches the elastic limit, the plastic zone will develop beneath the indenter as shown in Fig. 1. In the elastic-plastic regime, the mean contact pressure increases gradually. After the plastic zone expands to the surface of the specimen, the mean contact pressure increases slightly[4].

The true stress and true strain values determined from uniaxial tensile test data can be compared with both indentation stress – strain data according to the following equations[5]:

$$\sigma_{\text{indentation}} \approx p_m / \psi \approx \sigma_{\text{uniaxial tension}} \quad (1)$$

$$\varepsilon_{\text{ndentation}} \approx 0{,}2a / R \approx \varepsilon_{\text{uniaxial tension}} \quad (2)$$

where p_m is the mean contact pressure, R is the indenter radius, a is the contact radius and ψ is the constrain factor. In the elastic regime, the value of ψ increases linearly up to about 1.1. It increases gradually through the elastic-plastic regime, and is almost constant in the fully plastic regime[4].

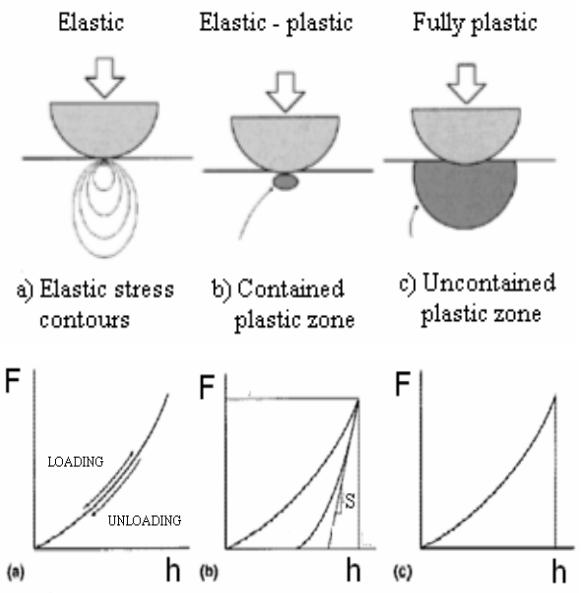

Fig. 1. **Schematic representation of plastic zone expansion during ball indentation[4]**

This paper deals with the determination of true stress – true strain curve on two materials, aluminium AA6063 and steel St 52, and with the comparison of the results from indentation with those of uniaxial tensile test.

2. Materials and experimental methods

The indentation experiments were performed using a NanoIndenter XP with the CSM (Continuous Stiffness Measurement) technique[6]. The spherical indenter tip of 600 μm diameter were made of ruby. For each sample, 10 measurements were performed and the average value was calculated. The uniaxial tensile test was performed using FP 100/1 tensile testing machine. The result of the tensile test is a force – extension, $F - \Delta L$ diagram, from which engineering stress, R, and strain, ε, were obtained using the following formulas:

$$R = \frac{F}{S_o} \quad (3)$$

$$\varepsilon = \frac{\Delta L}{L_o} \quad (4)$$

where F is the loading force, S_o is a specimen cross-section area, ΔL is the elongation, $L = L_o + \Delta L$.
The true stress, σ, and true strain, Φ, values were calculated according to equations:

$$\sigma = R\,(1+\varepsilon) \qquad (5)$$

$$\Phi = \ln\,(1+\varepsilon) \qquad (6)$$

3. Results and Discussion

3.1. Indentation tests

Typical indentation curves from single loading-unloading tests for both materials studied are illustrated in Fig. 2. These tests provide only one value of hardness and indentation modulus from each measurement.

However, when using the CSM method, the dependencies of hardness, H, and indentation modulus, E´, on the indentation depth, h, can be obtained (Fig. 3 and Fig. 4, respectively). As it can bee seen, E´ and H measured by

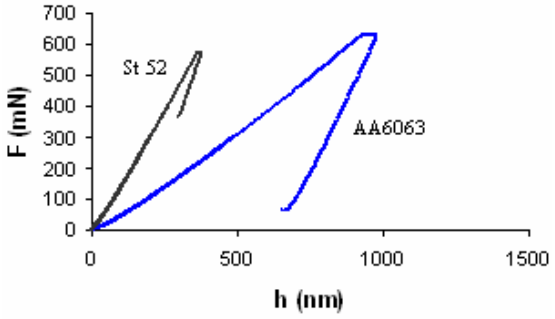

Fig. 2. **Indentation curves for AA6063 and St 52**

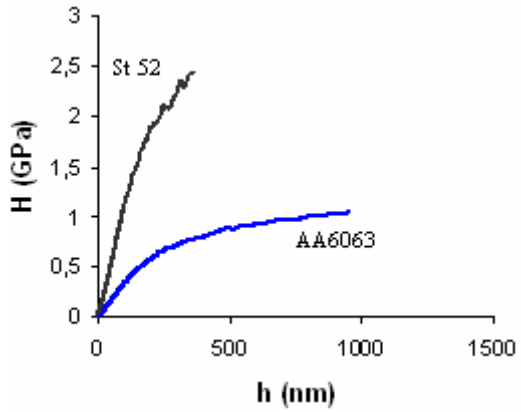

Fig. 3. **Dependence of hardness, H, on the indentation depth, h, for AA6063 and St 52**

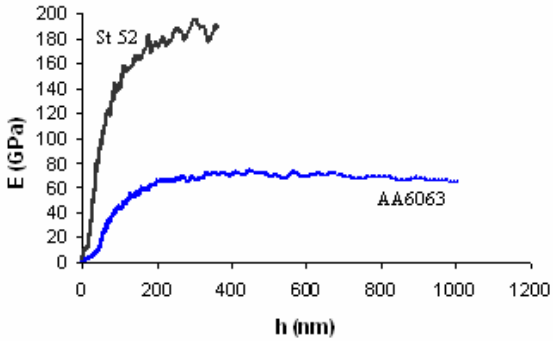

Fig. 4. **Dependence of indentation modulus E´ on the indentation depth for AA6063 and St 52**

CSM method rise from zero until saturation values. They correspond to typical values for both, aluminium[7] and steel[8].

It is also known that the values of indentation modulus E´ are influenced by the effects of pile-up or sinking-in[2] of the material around the indentation. The agreement between the measured and literature data indicate that these effects are not important in our case and confirm the correctness and reliability of current DSI measurements. On the other side, the first contact of the indenter with the specimen surface is usually biased by significant measurement errors due to undefined indenter shape, surface roughness and shape function. Hence, the beginning of the curves (up to approximately 50 nm depth) is considered to be non –relevant[9].

The stress – strain curves, σ – ε, (Fig. 5 and Fig. 6) were calculated using the Eq. (*1*) and Eq. (*2*) for both materials. The corresponding curves are plotted in Fig. 5 and Fig. 6. No clearly defined yield strength points are visible on the curves. Note that only the parts of the curves extending slightly about the yield strength limits known for these materials from the literature are drawn because of significant plasticity of both materials.

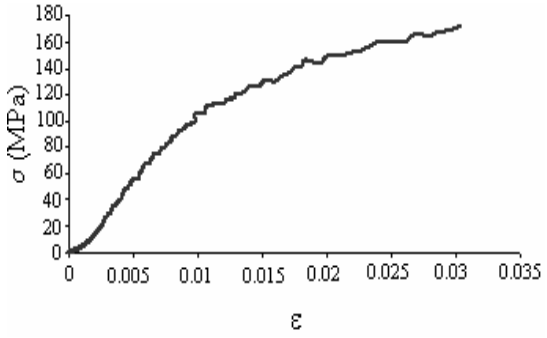

Fig. 5. **Stress σ – strain ε curve for aluminium AA6063**

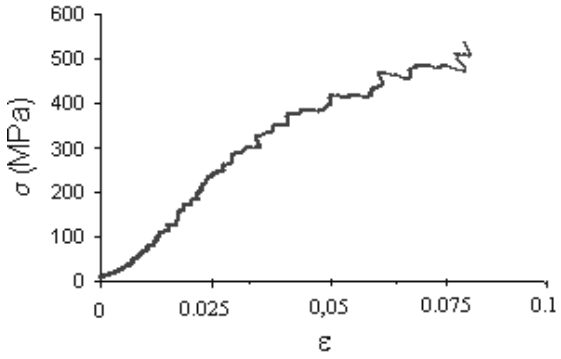

Fig. 6. **Stress σ – strain ε curve for steel St 52**

3.2. Uniaxial tensile tests

Fig. 7 a–b show the true and engineering stress – strain curves for both investigated materials obtained in uniaxial tensile tests. Yield strength is clearly defined in both cases and the differencies between true and engineering strains appear only at strain values exceeding 5 % strains.

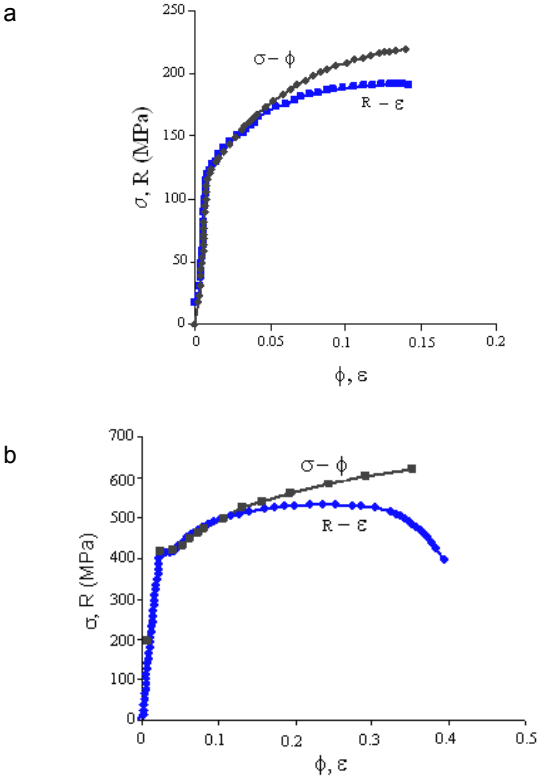

Fig. 7. **The engineering stress R – strain ε and true stress σ – true strain Φ curves for;** a) AA6063 b) St 52

3.3. Comparison of the results

The comparison of stress – strain curves obtained from uniaxial tensile testing and indentation testing for both materials is illustrated in Fig. 8 and Fig. 9, respectively. In the case aluminium, both curves are in good agreement in the elastic regime (Fig. 8). Curves differ in the elastic-plastic regime above the yield strength defined by tensile test. As discussed earlier, pile-up effects may cause deviations in contact area estimation. Subsequently, large differences may appear in contact stress determination and stress evaluation. The pile-up effect around the indent was not taken into account in our case, therefore, the deviations between both curves can be attributed to this effect.

The lack of pronounced yield strength limit on DSI curves in aluminium forced us to use $R_{p0,2}$ as a criterion. The corresponding data are summarized in Table I.

In case of St 52, the curves differ already in the elastic regime. It is known that this type of steel exhibits Luders deformation at the yield point which leads to strong

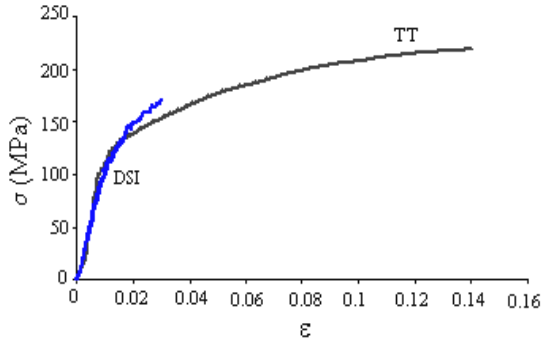

Fig. 8. **True stress σ – ε true strain curves for AA6063;** a) uniaxial tensile test (TT), b) indentation test (DSI)

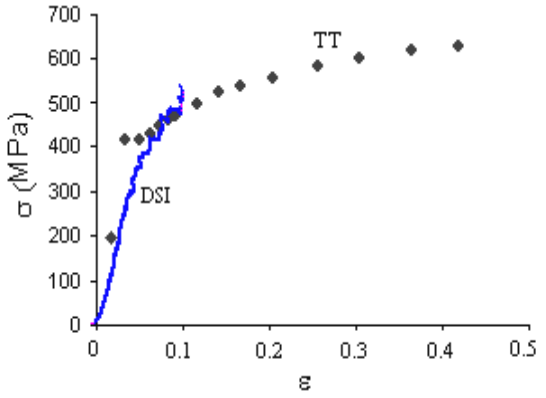

Fig. 9. **True stress σ – ε true strain curves for St 52;** a) uniaxial tensile test (TT), b) indentation test (DSI)

Table I
Values of yield strength

	AA6063 ($R_{p0,2}$) [MPa]	St 52 (R_e*, $R_{p0,2}$) [MPa]
Uniaxial tensile test	100	410*
DSI	110	450

pile-up. Quantifying of the pile-up effect is difficult and its absence in the evaluation of the stress – strain curve seems to result in the observed differences. However, despite the differencies already in the elastic regime, the yield strength values obtained from DSI based on $R_{p0.2}$ approach and from the tensile tests differ within 10 %.

4. Conclusions

The comparison of uniaxial tensile tests and DSI with spherical indenter using CSM method on aluminium AA6063 and steel St 52 revealed acceptable agreement between the stress – strain curves obtained from both techniques. The yield strength can be estimated from the stress – strain curve calculated from DSI/CSM technique using $R_{p0,2}$ approach. The obtained values exceed by 10% the values obtained from tensile tests. The deviations were attributed the unaccounted pile-up effects.

The values of indentation modulus measured by DSI are in good agreement with the real values of the Young´s modulus of both materials.

DSI technique with spherical indenter is a promissing method to determine stress – strain curves of bulk materials in case of lack of experimental material for tensile testing.

This work was supported by the Scientific Grant Agency of Slovak republic under the following grant projects: Slovak-Czech bilateral co-operation SK-CZ-0108-07, VEGA project No. 1/0846/09 and VEGA project No. 2/0138/10.

REFERENCES

1. Fischer-Cripps A. C.: *Nanoindentation*. Springer, New York 2002.
2. ISO 14577: 2001, *Metallic materials-Instrumented indentation test for hardness and materials parameters*, Part 1: test method, International organization for Standardization, 2001.
3. Tabor D.: *The Hardness of Metals*. Clarendon Press, Oxford 1951.
4. Choi Y., Kwon D.: *Derivation of tensile flow properties of thin films using nanoindentation technique*, pp. 525–531. Elsevier, Current Applied Physics 2, 2002.
5. Herbert E. G., et al.: *On the measurement of stress-strain curves by spherical indentation*. In: Mat. Res. Soc. Symp. Proc., Vol. 649, MRS, 2001.
6. *Nanoindenter XP Manual*, MTS Innovation Center, 2004.
7. Aalco: Aluminium alloys [online] 1. May 2000 [Quoted on 23.March 2009]. Available at http:// www.azom.com.
8. *Product catalogue*, Výskumný a skúšobný ústav, VSŽ oceľ 95/96.
9. Zubko P.: *PhD. Thesis*. Technical University, Košice 2007.

P. Gavendová[a], P. Zubko[b], L. Pešek*[b], and O. Bláhová[c] *([a] Institute of Materials Research, Slovak Academy of Sciences, Košice, Slovakia [b] Department of Materials Science, Technical University of Košice, Faculty of Metallurgy, Košice, Slovakia [c] New Technologies-Research Centre, University of West Bohemia, Plzeň, Czech Republic):* **Determining the True Stress-Strain Relationship by Depth Sensing Indentation on Two Construction Materials**

The aim of this paper is the determination of the true stress – true strain, σ – ε, curves by depth sensing indentation (DSI) on both aluminium (AA6063) and steel (St 52) using a spherical indentation. Hardness, H, indentation modulus, E´, and a part of the indentation stress – strain, σ – ε, curve were determined using a spherical indenter with 600 μm diameter using a NanoIndenter XP with CSM technique. Yield strength was defined as $R_{p0,2}$ for DSI. Uniaxial tensile test were performed for comparison of both techniques. The stress – strain curves obtained on basis of DSI technique agree within 10% accuracy with the values obtained from tensile tests. The deviations were attributed the unaccounted pile-up effects.

LOCAL ASPECTS OF SHEAR-MODE CRACK PROPAGATION IN AUSTENITIC STEEL

LIBOR HOLÁŇ, JAROSLAV POKLUDA, and KAREL SLÁMEČKA*

Brno University of Technology, Faculty of Mechanical Engineering, Technická 2, 616 69 Brno, Czech Republic
slamecka@fme.vutbr.cz

Keywords: shear cracks, local roughness, crack growth rate, growth micromechanisms, austenitic steel

1. Introduction

While the principal micromechanisms of fatigue crack growth under modes I and II are well known, there is a lack of any plausible interpretation in case of a pure mode III crack propagation[1]. Most of experiments allowing mode II and mode III crack propagation were performed in a pure torsion or asymmetrical 4-point bending (e.g. in ref.[2–8]). Except for the paper by Nayeb-Hashemi et al. [4], however, no detailed examinations of the micromechanism of shear mode crack growth were reported in these studies. Therefore, the investigation of shear crack growth mechanisms constitutes a rather big challenge.

A careful fractographical observation of mode II and III growth under pure shear remote loading in the region of very low cycle fatigue were performed by Pokluda et al.[9]. These investigations indicated that the microscopic mode of the pure remote mode II crack extension was rather a mixed I+II mechanism. Similarly, the mode II and the combined mode I+II were dominating microscopical fracture micromechanisms also during the remote mode III loading. The crack growth rate in mode II was found to be about five times higher than that in mode III (ref.[9]).

This paper presents a study on the near-threshold crack propagation under shear modes II and III. In this case, the local (microstructural) effects on the crack growth are dominant since the size of the cyclic plastic zone at the crack tip becomes less than that of a characteristic microstructural distance[10,11]. The crack flanks are, therefore, microscopically tortuous and related friction forces extremely rise and diminish the shear-mode crack driving force. As a consequence, the crack tip might tend to incline to a mode I loading by creating local mode I branches. Such cracks can no longer be considered to grow under a shear mode loading and measured "shear-mode" fatigue characteristics become irrelevant. In order to identify such processes, a local three-dimensional analysis of the fracture surface topology in a microscopic region close to the precrack tip had to be performed by means of the SEM stereo-photogrammetry.

2. Experimental arrangements and methods

Two original testing setups (cells) have been designed and utilized in order to assure both pure remote shear modes II and III crack propagation in a single cylindrical specimen. The loading scheme of the first cell is depicted in Fig. 1. The cracks at the "top" and "bottom" sites of the specimen grew under a pure mode II loading while those at the "front" and "back" sites propagated under a pure mode III loading (the mixed mode II+III in all other crack front points). A circumferential V-notch was machined by a lathe tool at the specimen mid-length and a precrack was introduced by a blade mechanism. Finally the specimens were compressed by 20 kN to sharpen the precrack. Five specimens made of the austenitic steel X5NiCrTi26-15 with the outer diameter of 8 mm and the inner diameter of 4 mm were tested by using the shear stress loading range of 180 MPa and the cyclic ratio $R = 0.1$.

The second special cell for loading specimens was manufactured to enable higher loadings (see Fig. 2). Five specimens with the outer diameter of 25 mm and the inner diameter of 12 mm were tested by using the $\Delta\tau_n$-values of 160 MPa (2 specimens), 200 MPa (2 specimens) and 220 MPa (1 specimen) and the cyclic ratio $R = 0.1$. After the shear mode tests, all specimens were fractured by the cyclic tensile loading.

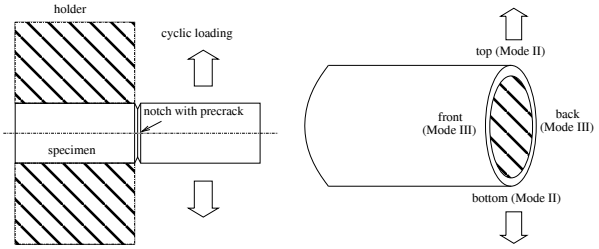

Fig. 1. **The loading scheme for small specimens and, the loading modes operating at different specimen sites**

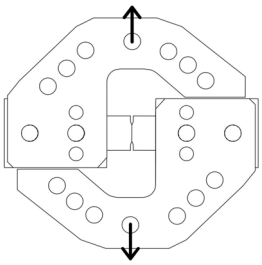

Fig. 2. **The scheme of the loading cell. The loading direction is indicated**

In order to determine the mode II and mode III stress intensity factors at the crack tip, a numerical analysis was performed by means of the ANSYS code[12].

The spatial crack tortuosity in a close vicinity of the precrack was determined by means of the stereo-photogrammetry in the scanning electron microscope (SEM). The stereo-photogrammetry is a method that makes use of the stereoscopic principles in order to obtain topographical data of fracture surface under investigation. Inputs of the method are two images of the analyzed region taken from different positions of view (so-called stereoimages, stereopair) and some additional parameters that characterize a projection used during their acquisition. Usually, SEM equipped with the eucentric holder is employed and the stereopair is obtained by tilting the specimen in the microscope chamber by an angle that depends on a local roughness of the surface. The stereopair is processed via a matching algorithm in order to find corresponding points on both images (homologue points) and the relative *z*-coordinates of homologue points are calculated. The 3D model of depicted surface area usually consists of 10–20 thousand non-equidistant points and so called Delaunay triangulation must be performed[13].

3. Theoretical and experimental results

In order to determine the mode II and mode III stress intensity factors at the crack tip, a numerical analysis was performed by means of the ANSYS code[12]. Although the loaded specimen was modelled as a rotationally symmetric, a full linear-elastic 3D solution had to be used owing to a different symmetry of the loading. Very precise values of the stress intensity factors K_I, K_{II} and K_{III} could be calculated in this way. The ratio of maximal values in pure shear modes II and III was found to be $K_{IIImax}/K_{IImax} = 1.37$ and the values of K_{Imax} were found to be negligible (in two orders lower). The results of this theoretical analysis were used to determine stress intensity factors for all experimental specimens investigated in this study.

Typical two-dimensional fracture morphology of pure mode II and III shear cracks is shown in Fig. 3. In this figure, the regions corresponding to a precrack, shear mode propagation and final fracture are highlighted as white boundaries. Since the length of the shear mode cracks was an order lower than that of the pre-crack, a nearly constant crack growth rate during the shear propagation could be assumed. Therefore, the crack-growth-rate was calculated simply by dividing the total length of shear cracks by corresponding numbers of cycles. The near-threshold crack growth curves for both the mode II and the mode III propagation in the austenitic steel are plotted in Fig. 4. The related regression curves follow the Klesnil-Lukas relationship $da/dN = A\left(\Delta K^n - \Delta K_{th}^n\right)$ (ref.[14]). The fatigue thresholds $\Delta K_{IIth} = 3.5$ MPa m$^{1/2}$ and $\Delta K_{IIIth} = 4.7$ MPa m$^{1/2}$ are different ($A_{II} = 1.13 \cdot 10^{13}$, $A_{III} = 2.72 \cdot 10^{13}$ – calculated from inputs in MPa, m units). On the other hand, the exponents are similar ($n_{II} = 5.6$, $n_{III} = 5.1$). One can also clearly see that, for the same value of the applied ΔK range, the crack growth rates for the mode II loading are about 6 times higher than those for the mode III loading. This is in agreement with results achieved in the low-cycle fatigue region[9] and confirms the diversity of the mechanisms of mode II and mode III crack propagation in metals[1].

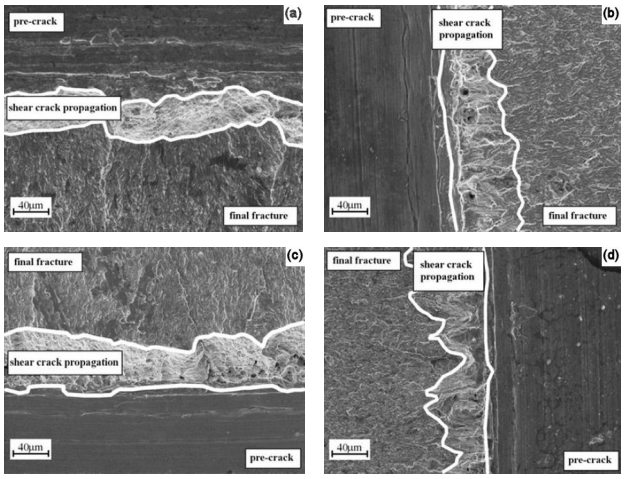

Fig. 3. **Typical fracture surfaces:** (a) top (mode II), (b) front (mode III), (c) bottom (mode II), (d) back (mode III)

Typical fracture morphology and local topology profiles related to both mode II and III cracks near the pre-crack tip are shown in Fig. 5. This figure shows a big topological difference between mode II and III cracks. Indeed, practically all the mode II shear crack fronts were globally inclined from the shear plane in the direction perpendicular on the crack front. This means that the mode II cracks immediately started to propagate under a local mode I in order to avoid the retarding friction stress. Averaged de-

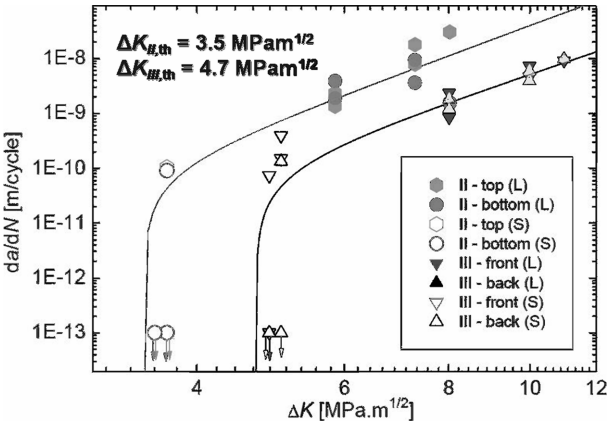

Fig. 4. **The crack-growth rate curves for mode II and III in the near-threshold region;** (S) – small specimens, (L) – large specimens

flection angles in the direction perpendicular to the crack front were found to be of 54°±16°. The roughness of inclined branches was very low and the associated crack path was microscopically smooth. This means that the roughness-induced crack closure was negligible and the cracks could propagate under a rather high effective crack driving force in the local mode I. On the other hand, the roughness of fracture surfaces of mode III cracks was extremely high and the related morphology typically consisted of factory-roof patterns. The deflection angles of factory roof micro-walls were in the range of 48°±9°. Because the mode III shear displacements were oriented perpendicularly to these asperities, their strong interlocking (clinching) took place during the cyclic loading. The theory of interaction of factory-roof asperities[15] shows that the roughness-induced closure produced in such a way diminishes the crack driving force to a very low level particularly in the near threshold region. This is the main reason why the crack growth rate under the remote mode III was found to be much lower than that under the mode II in spite of the fact that both kinds of cracks propagated locally along the mode I branches.

It should be emphasized that no local measurements of 3D micromorphology were performed before the publication of the paper[1]. Thus, a majority of previously published values of the shear-mode crack growth thresholds (e.g. in ref.[7]) are, most probably, irrelevant since they correspond to mode I branches. In order to achieve real shear-mode propagation at least at its initiation stages, the precrack tip must be made as sharp as possible which enables to constrain the crack tip plastic zone to a narrow strip within the shear plane. Moreover, the roughness of precrack flanks near the crack tip must be substantially diminished in order to avoid a parasitic mode I loading induced by a bending contact of asperities localized near the crack tip. Such precracks were produced in the Erich-Schmid Institute of Materials Science in Leoben, Austria, by

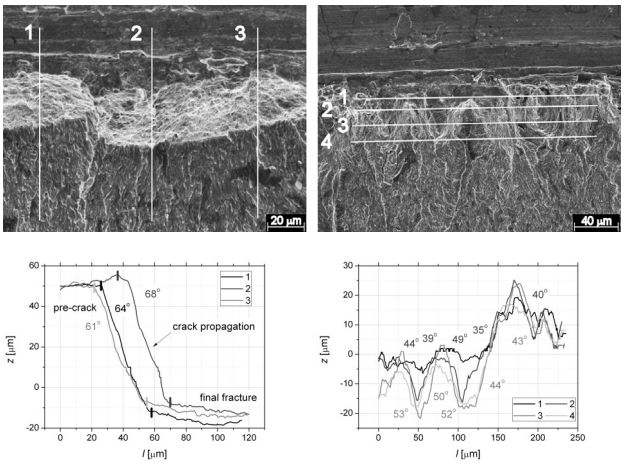

Fig. 5. **SEM images and related height profiles for mode II (left) and mode III (right) crack propagations**

Table I
Roughness analysis

	R_q [μm]	R_L [−]	R_V [−]
Original precrack	2.15±1.15	1.27±0.65	0.57±0.70
New precracks	0.87±0.47	1.08±0.03	0.32±0.08

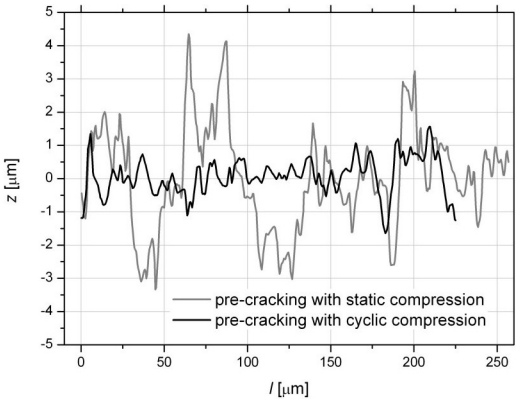

Fig. 6. **Height profiles of the surface roughness near the crack front for the original precracks (static compression) and the new ones (cyclic compression)**

means of a generation of a short fatigue precrack under compressive cyclic loading. In order to compare the local roughness of original and new precracks, the stereogrammetrical roughness analysis was performed on both types of precracks. The investigated parameters were the root mean square roughness (standard deviation of height coordinates), R_q, the linear roughness, R_L, defined as the ratio of the true profile length L and its projected length L', and the vertical roughness R_V, calculated as $R_V=h/L'$, where h is the sum of height differences between adjacent profile points.

A comparison of local roughness in the z-direction (heights) and the roughness parameters for both types of precracks is shown in Fig. 6 and Tab. I, respectively. The profiles after cyclic compression become substantially smoothed, as can be seen from Fig. 6. All of the investigated roughness parameters for the new precracks are also significantly lower than those for the original ones. By means of such precracks, indeed, sufficiently extended shear-mode crack propagation has been already achieved. The assessment of the related experiments is currently in progress.

4. Conclusion

A prototype experiments on the near-threshold crack growth enabled a simultaneous remote mode II and mode III fatigue crack growth in specimens made of the austenitic steel. The stereo-photogrammetrical analysis of

the microroughness near the precrack tip revealed that, in both remote mode II and III cases, the cracks propagated under the local opening mode I. The main results of the study can be summarized in the following points:

(i) The near-threshold crack growth rate under the remote mode II was much higher than that under the remote mode III. The threshold value ΔK_{IIth} was found to be of 3.5 MPa $m^{1/2}$, whereas $\Delta K_{\mathrm{IIIth}} \approx 4.7$ MPa $m^{1/2}$ was determined.

(ii) All cracks propagated under the local mode I loading by forming either deflection of the whole crack front (mode II) or the factory roof patterns (mode III). Therefore, the measured crack-growth data can not be considered to be shear- mode material characteristics.

(iii) The difference in the crack growth rate under modes II and III can be explained by a significant difference in the related micromechanisms. While the fracture topology of mode II cracks is smooth, that of the mode III cracks is rough which causes an interlocking of crack-flank asperities localized near the crack front. This significantly reduces the effective crack driving force for the mode III loading.

In general, the results of the local approach to shear-mode crack growth have shown that a majority of previously published values of mode II and III thresholds are irrelevant since they, most probably, correspond to mode I branches.

This research was supported by the Ministry of Education, Youth and Sports of the Czech Republic in the frame of projects MSM 0021630518 and project NPVII-2E08017. Authors greatly appreciate the help of Prof. Reinhard Pippan and Anton Hohenwarter from the Erich-Schmid Institute of Materials Science, Austrian Academy of Sciences, who significantly contributed to the development of experimental device as well as to the assessment of fractographic data.

REFERENCES

1. Pokluda J., Pippan R.: Fat. Fract. Engng. Mater. Structures *28*, 179 (2005).
2. Ritchie R. O., McClintock F. A., Nayeb-Hashemi H., Rittler M. A.: Metall. Trans. *A13*, 101 (1982).
3. Tschegg E. K.: Mater. Sci. Eng. *A54*, 127 (1982).
4. Nayeb-Hashemi H., McClintock F. A., Ritchie R. O.: Int. J. Fracture *23*, 163 (1983).
5. Hellier A. K., Corderoy D. L. H., Mc Girr M. B.: Int. J. Fatigue *9*, 95 (1987).
6. Hellier A. K., McGirr M. B., Cordero D. J. H., Kutajczyk L. A.: Int. J. Fracture *42*, R19 (1990).
7. Pook L. P.: *Crack Paths*. Wit Press, London 2002.
8. Murakami Y.: *Metal fatigue: Effects of small defects and nonmetallic inclusions*. Elsevier, Amsterdam 2002.
9. Pokluda J., Trattnig G., Martinschitz C., Pippan R.: Int. J. Fatigue *30*, 1498 **(**2008).
10. Pokluda J., Pippan R.: Mater. Sci. Eng. *A462*, 355 (2007).
11. Pokluda J., Kondo Y., Slámečka K., Šandera P., Horníková J.: Key Eng. Mater. *385-387*, 49 (2008).
12. Horníková J., Šandera P., Pokluda J.: Key Eng. Mater. *417-418*, 321 (2010).
13. Slámečka K., Pokluda J., Ponížil P., Major Š., Šandera P.: Eng. Fract. Mechanics *75*, 760 (2008).
14. Klesnil M., Lukas P.: *Fatigue of Metallic Materials.* Elsevier, Oxford 1980.
15. Vaziri A., Nayeb-Hashemi H.: Eng. Fract. Mechanics *72*, 617 (2005).

L. Holáň, J. Pokluda, and K. Slámečka *(Brno University of Technology, Faculty of Mechanical Engineering):* **Local Aspects of Shear-Mode Crack Propagation in Austenitic Steel**

Two prototype experiments allowing a simultaneous mode II and mode III fatigue crack propagation in a single specimen are described and discussed. The cylindrical specimens made of austenitic steel with circumferential V-notch were prepared. In order to indicate differences between the mechanisms of mode II and mode III crack growth, several roughness parameters were determined by a stereo-photogrammetrical analysis within a microscopic region on the fracture surface close to the artificial precrack. The analysis revealed that both macroscopically shear-mode cracks propagated locally under the opening mode I loading. Unlike in the mode II case, moreover, an intensive interlocking of large asperities took place during the mode III crack growth. Therefore, the mode III crack-growth threshold (crack-growth-rate) was found to be higher (lower) than the mode II one. The results also revealed that, in order to achieve a local shear-mode growth, new experiments using specimens with sharper and microscopically smoother precracks must be arranged.